

Printing Reconfigurable Bundles of Dielectric Elastomer Fibers

Alex Chortos, Jie Mao, Jochen Mueller, Ehsan Hajiesmaili, Jennifer A. Lewis, and David R. Clarke*


Active soft materials that change shape on demand are of interest for a myriad of applications, including soft robotics, biomedical devices, and adaptive systems. Despite recent advances, the ability to rapidly design and fabricate active matter in complex, reconfigurable layouts remains challenging. Here, the 3D printing of core-sheath-shell dielectric elastomer fibers (DEF) and fiber bundles with programmable actuation is reported. Complex shape morphing responses are achieved by printing individually addressable fibers within 3D architectures, including vertical coils and fiber bundles. These DEF devices exhibit resonance frequencies up to 700 Hz and lifetimes exceeding 2.6 million cycles. The multimaterial, multicore-shell 3D printing method opens new avenues for creating active soft matter with fast programmable actuation.

1. Introduction

Active soft materials that change shape^[1–14] are widely used in soft robotics,^[2,3,13] biomedical devices,^[10,15] and adaptive systems.^[7–9,11,16,17] They can morph into pre-determined shapes^[1,7,16–19] in response to external stimuli, e.g., temperature,^[20] humidity,^[7,21] optical,^[22,23] or electrical^[8,24] signals. Dielectric elastomer actuators (DEAs) represent one important class of active soft matter. They exhibit fast, efficient shape-morphing behavior by converting electrical to mechanical energy using electrostatic forces to deform soft capacitive elements.^[25,26] [8,27–29] To date, most DEAs have been fabricated in planar motifs, such as prestretched elastomer membranes sandwiched between compliant electrodes.^[25,30] While planar DEAs can be fabricated using high-throughput roll-to-roll manufacturing^[31] or automated sequential stacking processes,^[32] these methods do not allow complex 3D architectures to be realized. By contrast, 3D printing of DEAs has recently been used to create 3D DEAs in the form of high-aspect ratio, interdigitated architectures.^[29,33–37] Unlike light-based 3D printing,^[37] direct ink writing enables complex architectures to be patterned from single^[38] and multiple materials^[39–40] via extrusion of viscoelastic inks through nozzle-based printheads.

Dr. A. Chortos, J. Mao, J. Mueller, E. Hajiesmaili, Prof. J. A. Lewis, Prof. D. R. Clarke
John A. Paulson School of Engineering and Applied Sciences
Harvard University
Cambridge, MA 02138, USA
E-mail: clarke@seas.harvard.edu

Dr. A. Chortos, J. Mueller, Prof. J. Lewis
Wyss Institute for Biologically Inspired Engineering
Harvard University
Cambridge, MA 02138, USA

 The ORCID identification number(s) for the author(s) of this article can be found under <https://doi.org/10.1002/adfm.202010643>.

DOI: 10.1002/adfm.202010643

Here, we build upon our prior work to create modular actuating elements via multimaterial, multicore-shell 3D printing^[41,42] in which insulating dielectric matrices and conductive electrodes are co-extruded to form coaxial dielectric elastomer fibers (DEFs) (Figure 1a). Prior efforts to create DEFs relied on manual coating of electrodes onto fixed lengths of hollow dielectric elastomer tubes.^[43–48] By contrast, our approach allows DEFs of locally programmed composition to be constructed in arbitrary designs by switching the core, sheath, and shell inks on and off during printing (Figure 1a). As

exemplars, we fabricated vertical coils (Figure 1b) and bundles (Figure 1c), in which each DEF is individually addressable to enable complex programmable actuation.

2. Results and Discussion

2.1. Dielectric Matrix and Electrode Inks

We created both dielectric matrix and electrode inks for DEF printing. Each ink is tailored to have the requisite viscoelasticity for printing high performance DEF-based architectures. These inks readily flow through the nozzle when the applied shear stress (τ) exceeds its shear yield stress (τ_y) yet return to a solid-like state (i.e., the storage modulus, G' , exceeds the loss modulus, G'') under quiescent conditions upon exiting the nozzle.^[49,50] The printed DEFs must maintain their concentric architecture with consistent dielectric thicknesses to achieve the desired actuation performance even when patterned in high aspect ratio 3D architectures, such as vertical coils (Figure 2a). The electrical (i.e., dielectric constant and conductivity, respectively) and mechanical properties (i.e., low shear modulus and low mechanical losses) of the cured dielectric matrix and electrode inks must also be tailored to achieve a fast, efficient actuation response.

To meet the above criteria, we created a dielectric matrix ink composed of Ecoflex silicone (Eco30) and 10.7 wt% PDMS-functionalized fumed silica, which serves as a rheological modifier. We further tailored the ink rheology by adding silicone (SE1700),^[2] which substantially increases the plateau G' and τ_y (Figure 2b). By combining silica-filled Eco30 and SE1700, we achieved a favorable tradeoff between the print fidelity of the uncured silicone-based ink and the mechanical properties of the cured dielectric elastomer matrix (Table 1). When the plateau G' of the uncured ink is comparable to the shear modulus of the cured elastomer matrix, the silica filler

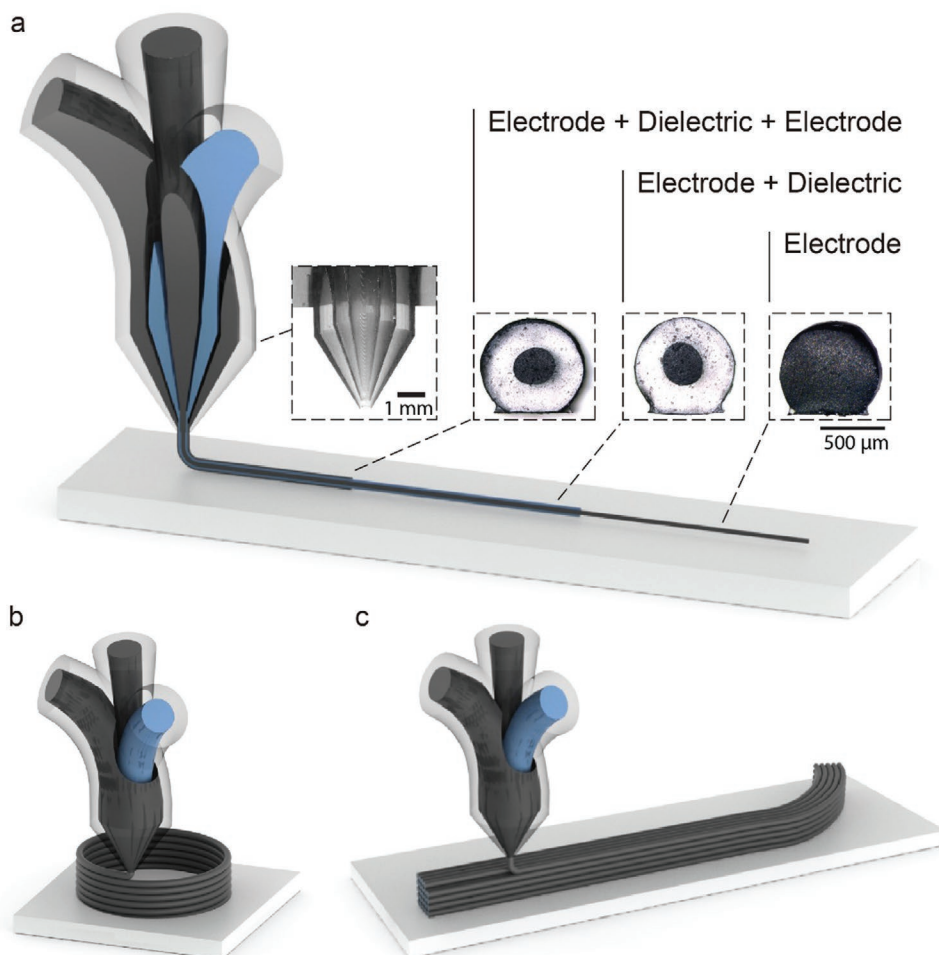


Figure 1. a) Schematic illustration of multimaterial, multicore-shell 3D printing, including cross-sectional view of nozzle-based printhead and coaxial dielectric elastomer fiber (DEF), optical images in combined reflected and transmitted light of the fiber cross-section highlight its multimaterial, multicore-shell geometry, b) vertical DEF coils, and c) DEF bundles.

network plays a dominant role in its viscoelastic response and subsequent mechanical losses that arise due to breaking and reforming the particle network. For example, lightly crosslinked SE1700 (30:1 ratio of base-to-crosslinker) exhibits a plateau G' of 191 kPa (uncured) and a shear modulus of 285.7 kPa (cured) resulting in a large $\tan\delta$ of 0.336 (Figure 2c). By comparison, highly crosslinked SE1700 (10:1 ratio) exhibits a shear modulus of 979 kPa and a $\tan\delta$ of 0.112 due to the increased contribution of the elastomer network to matrix stiffness. We find that dielectric matrix inks composed of 75 wt% silica-filled Eco30 and 25 wt% SE1700 exhibits optimal printing and mechanical performance, with relatively high yield stress of 0.316 kPa in the uncured state coupled with a shear modulus and $\tan\delta$ of 246.4 kPa and 0.155, respectively, in the cured state. The dielectric constant is calculated from the areal capacitance of parallel plate capacitors (Figure S2, Supporting Information) at 100 Hz. The measured value of 3.6 ± 0.25 is in good agreement with other silicone-based dielectrics.^[51,52]

Next, we created an electrode ink composed of an uncured silicone matrix (Eco30) and hydrophobic carbon black, which serves as both a rheological modifier and conductive filler. The

yield stress and plateau modulus increase with carbon black loading (Figure 2d). A carbon black filler content of 13.8 wt% results in a yield stress and plateau modulus of 0.316 and 44 kPa, respectively, which are comparable to those of the dielectric ink. Upon curing, these stretchable electrodes exhibit a tradeoff between their mechanical and electrical properties. With increasing carbon black content, the electrical conductivity and strain-dependent conductivity improve but at the expense of increasing shear modulus.^[53–55] For example, when the carbon black content is increased from 0% to 74 wt% (near electrical percolation) to 13.8 wt%, the Young's modulus increases from 81.6 to 177 to 288 kPa, respectively. Assuming a Poisson's ratio close to 0.5, the Young's modulus derived from tensile measurements (Figure 2e) is related to the shear modulus by a factor of $1/3$,^[56] giving rise to a shear modulus of 96 kPa for electrode inks with 13.8 wt% carbon black. This value remains below the shear modulus of the cured dielectric matrix, minimizing the extent to which these stretchable electrodes constrain device actuation. The electrical conductivity of the cured electrode ink with 13.8 wt% carbon black remains above 0.5 S m^{-1} within the strain range up to 100% (Figure 2f).

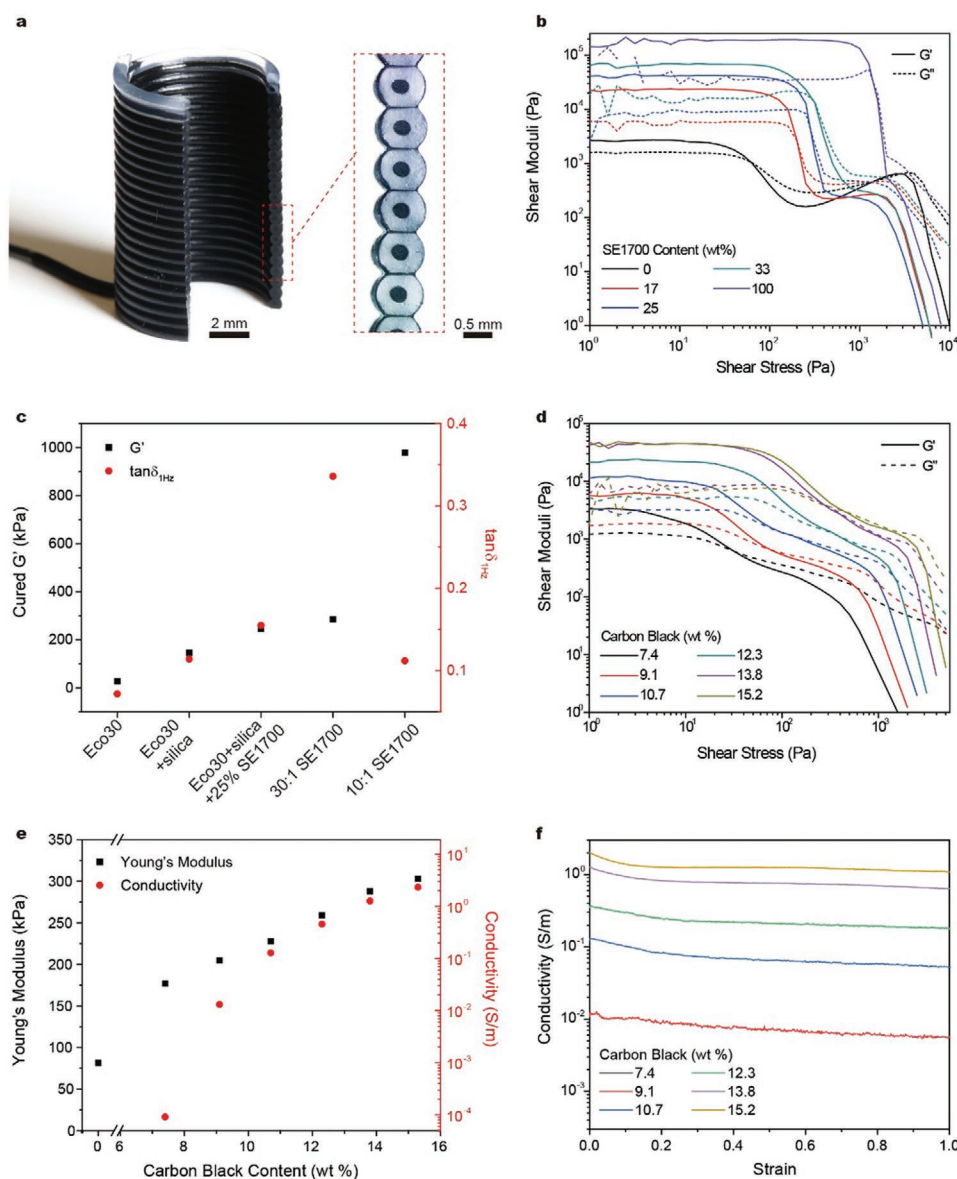


Figure 2. Dielectric matrix and electrode inks for DEF printing. a) Cross-sectional image of a vertical DEF coil (22 turns in height), b) log-log plot of shear moduli as a function of shear stress for uncured dielectric matrix inks of varying composition, c) shear modulus and $\tan \delta$ for cured dielectric matrices of varying composition. d) log-log plot of shear moduli as a function of shear stress for uncured electrode inks of varying composition, e) Young's modulus and electrical conductivity for cured electrode inks of varying composition, and f) semi-log plot of electrical conductivity as a function of strain for cured electrode inks of varying composition.

Table 1. Rheological and mechanical properties of dielectric matrix inks.

Composition	Uncured Ink		Cured Ink	
	Shear Yield Stress [kPa]	Plateau Modulus [kPa]	Shear Modulus [kPa]	$\tan \delta_{1\text{Hz}}$
Eco30	–	–	27.2	0.072
Eco30 + silica	0.063	2.69	146.4	0.114
75%Eco30 + silica + 25%SE1700	0.316	41.8	246.4	0.155
SE1700 30:1	1.585	190.7	285.7	0.336
SE1700 10:1	1.585	153.3	979	0.112

2.2. Dielectric Elastomer Fibers and Bundles

Single DEFs are fabricated using a multimaterial, multicore-shell 3D printhead (Figure S3, Supporting Information),^[41,42] which enables co-extrusion of dielectric matrix and electrode inks to form a coaxial fiber. Each DEF actuator consists of a dielectric elastomer sheath between an inner conductive core and an outer conducting shell (Figures 1 and 3a). Unlike hollow-core DEFs^[43–48] that expand radially and axially when a voltage is applied,^[45,47] our DEFs contain solid cores leading to qualitatively different behavior. When a voltage is applied between the inner and outer electrodes, the elastomer sheath in between is compressed by the radially acting Maxwell stress with the radial constraint imposed by the solid core. In response, our solid-core DEFs elongate along the axial direction, but contract radially (Figure 3a). We have developed an analytical model to predict the deformation of single dielectric elastomer fibers based on minimizing their combined electrostatic

and mechanical energies (Note S1, Supporting Information). By invoking the theory of virtual work,^[57–59] the actuation stretch, λ , along the fiber is related to the applied potential, V , and the radii of the core, sheath, and shell (Figure 3a) by

$$\lambda - \lambda^{-2} = \frac{\epsilon_0 \epsilon_r}{\mu R_3^2 \ln(R_2 / R_1)} V^2 \quad (1)$$

where ϵ_0 is the vacuum permittivity, ϵ_r is the relative permittivity, R_1 is the core electrode radius, R_2 is dielectric sheath radius, and R_3 is the outer fiber radius.

To experimentally explore fiber geometry effects on actuation performance, we created individual DEFs of varying core electrode diameter with a fixed fiber diameter of $\approx 730 \mu\text{m}$ and outer electrode thickness of $\approx 15 \mu\text{m}$ (Table S1, Supporting Information). The outer electrode is necessary to provide charges and induce the desired DEF actuation, but it acts as

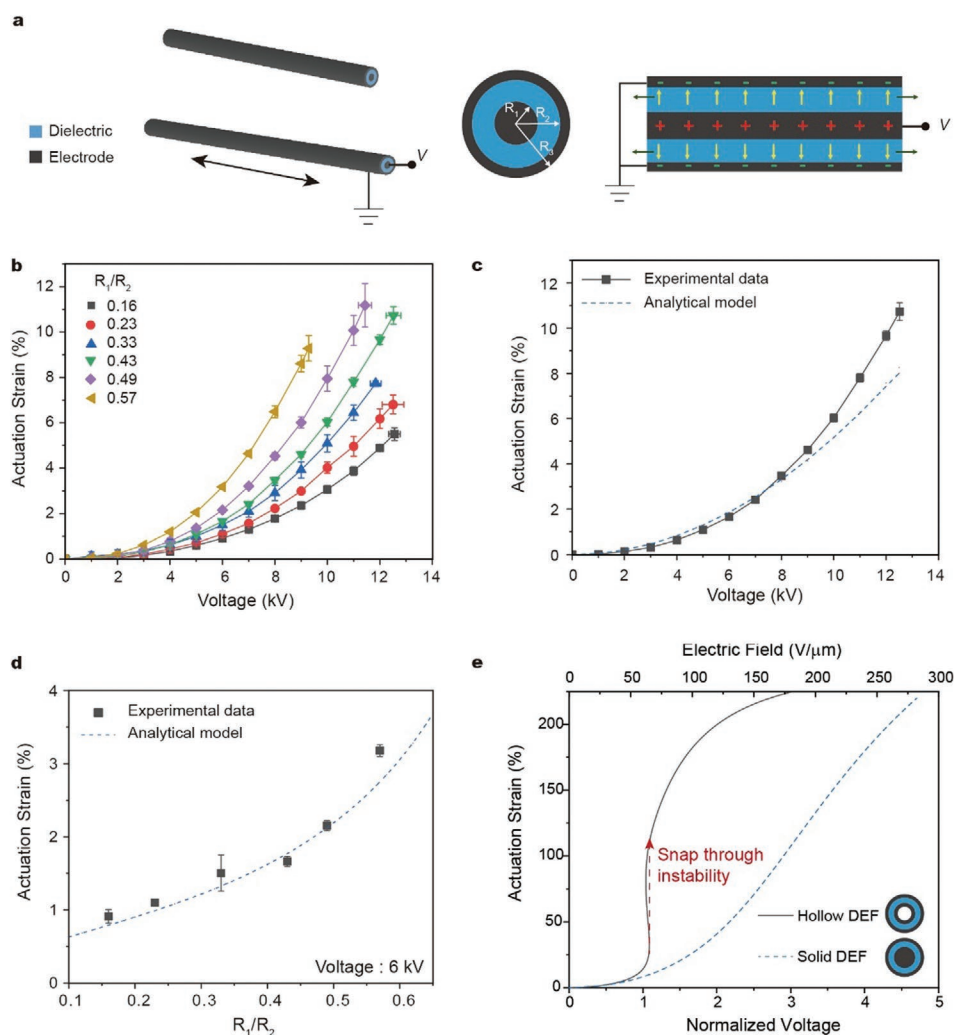


Figure 3. Actuation performance of individual DEFs. a) Schematic view of the actuation mechanism of our solid-core DEF under a radial electric field, b) longitudinal actuation strain as a function of voltage for DEFs having different R_1/R_2 ratios, c) experimental and predicted (from Equation S8 in the Supporting Information) actuation strain as a function of voltage and for a solid-core DEF with $R_1/R_2 = 0.43$, d) experimental and predicted actuation strain as a function of DEF geometry for at a voltage of 6 kV, and e) comparison between a hollow-core DEF^[47] and our solid-core DEF. The electric field in the top x-axis is calculated using materials constants of 115 kPa for μ and 3.6 for ϵ of our fibers.

a passive mechanical constraint. We found that a minimum thickness of 15 μm was required to achieve a uniform outer electrode. Controlling the print pressures enables the core and dielectric thicknesses to be varied over a large range.^[41] For example, we varied the dielectric elastomer layer thickness from 156 to 286 μm , yielding different radius ratios of R_1/R_2 from 0.57 to 0.19. The extruded DEFs exhibited consistent coaxial dimensions over this range of values, as shown in Figure S4 in the Supporting Information. The actuation voltage required to achieve a given strain decreases with increasing R_1/R_2 (Figure 3b), yet the actuation performance remains constant as a function of electric field (Figure S5b, Supporting Information). The breakdown strengths exceed 60 $\text{V } \mu\text{m}^{-1}$ (Figure S5c, Supporting Information), comparable to state-of-the-art silicone dielectric elastomer actuators.^[63] Yu and Skov^[64] describe a mathematical relationship between the breakdown strength and the Young's modulus of PDMS and find a good agreement with a range of commercial and custom PDMS formulations. Our dielectric composition, with a Young's modulus of 345 kPa, falls between that of a custom composition of linear PDMS chains (DMS-V41 with a modulus of 510 kPa and a breakdown strength of 66 $\text{V } \mu\text{m}^{-1}$) and a custom bottlebrush PDMS composition (SE1 with a modulus of 370 kPa and a breakdown strength of 30 $\text{V } \mu\text{m}^{-1}$).

The analytical model (using materials constants shown in Figure S6 in the Supporting Information) accurately predicts the quadratic dependence of strain with voltage and is consistent with experimental observation up to $\approx 4\%$ strain (Figure 3c). At larger strains (≈ 8 kV), the experimental results diverge from the analytical and FEM models, possibly due to a Poisson's ratio that diverges from the ideal value of 0.5 for highly filled elastomers. For a constant applied voltage of 6 kV, the actuation strain increases with increasing R_1/R_2 (Figure 3d). We note that the electromechanical performance of our printed DEFs are comparable to values reported for other dielectric elastomer fibers (Table S2, Supporting Information). The axial actuation strain of our DEFs of $\approx 10\%$ is comparable to the largest strain reported in previous DEA fibers.^[44]

We experimentally investigated the behavior of DEF devices with constraints (modulus and breakdown field) arising from our materials and solid-core fiber geometry; however, the model allows one to predict actuation properties for other DEFs. Significant improvements could be realized by increasing the dielectric constant and breakdown field of the matrix^[65] and additives used.^[66,67] For example, block copolymers^[68,69] and microgels^[70] can be used as printable shear-thinning materials with lower shear moduli (μ) to increase the actuation strains. This analytical model also reveals that solid-core, coaxial DEFs are not susceptible to electromechanical instability that typically leads to failure of hollow-core DEFs^[47] and planar DEAs^[60–62] (Figure 3e). The theoretical relationship between voltage and strain is non-monotonic for hollow-core DEFs, resulting in an electromechanical instability above a critical actuation whereby the dielectric abruptly thins, resulting in electrical failure. In planar DEAs without pre-strain, this instability occurs at 26% actuation strain for Neo-Hookean elastomers. In hollow-core DEFs, the strain at which this instability arises decreases as the externally imposed strain in the actuator increases, reaching as low as 10% for large pre-strains.^[47]

Multimaterial, multicore-shell 3D printing enables the scalable fabrication of DEF bundles with increased total force output compared to individual fiber actuators. Since these actuators extend upon applying a voltage, they produce useful work when operated in tension. We define the “restrained force” as the change in force while applying a voltage to a bundle of fibers that is held at a fixed strain of 10% (Figure 4a). As expected for parallel fibers, this force increases linearly as the number of fibers in the bundle increases (Figure 4b; Figure S7, Supporting Information). We characterized the ability of the actuators to do work by measuring the free displacement of a hanging bundle with different loads (Figure 4c). During quasi-static actuation of a 5×5 bundle, the actuator achieves 3% strain at 8 kV with a load of 52.8 g and exhibits a peak energy density at a load of 102.5 g (Figure 4d; Figure S8, Supporting Information). Akin to other mechanical devices,^[4,71] the displacement of the bundle actuator increases near resonance. For example, this DEF bundle exhibits a linear actuation strain of 12% near the resonant frequency (4 Hz) under a load of 72.8 g (Figure 4e; Figure S9 and Video S1, Supporting Information). Compared to other soft actuators (e.g., liquid crystal elastomers^[74]), DEAs exhibit higher efficiency, bandwidth, and strain, while having limited actuation stress and power density. The specific power for our DEFs of 134 W kg^{-1} is comparable to other DEA devices, such as hydraulically amplified electrostatic actuators with power densities of 102^[75] and 614 W kg^{-1} ^[4] and thin-film devices with power densities of 100–1000^[30] and 600 W kg^{-1} .^[72] Note that our power density is reported at a resonance frequency of 4 Hz; designing smaller structures that have higher resonance frequencies could significantly improve the reported power density without changing the DEF materials or printing process.

2.3. Programmable and Reconfigurable DEF Actuators

Our 3D printing technique enables DEF fibers to be patterned in out-of-plane motifs, which are capable of programmed shape-morphing responses. As one example, we produced vertical coil actuators composed of a single DEF that expand radially and contract axially when actuated (Figure 5a). The radial strain in the cylindrical coil actuation geometry varies as the square root of the fiber axial strain. Our vertical coil actuators (wall thickness \approx diameter of a single DEF; 15 fiber layers in height) exhibit a bandwidth of 45 Hz (defined as the frequency where the amplitude reaches $\sqrt{2}/2$ of the static amplitude) and a resonance frequency of about 700 Hz (Figure 5b), which is several orders of magnitude higher than other active matter produced by 3D printing (<10 Hz)^[1,7,18] and comparable to state-of-the-art dielectric elastomer actuators (>100 Hz).^[71,72] Their bandwidth is limited by mechanical loss in the elastomers as well as electrical losses in the electrodes.^[71] The low-field capacitance of the vertical coil actuator has a bandwidth of 632 Hz (Figure S10, Supporting Information), suggesting that the electrodes are sufficiently conductive to charge and discharge individual DEF and that their response is primarily limited due to viscoelastic losses of the materials used. The vertical coil consists of a total fiber length of 65 mm. For coaxial cables, the RC time constant is expected to be proportional to L^2 , where L is the length of

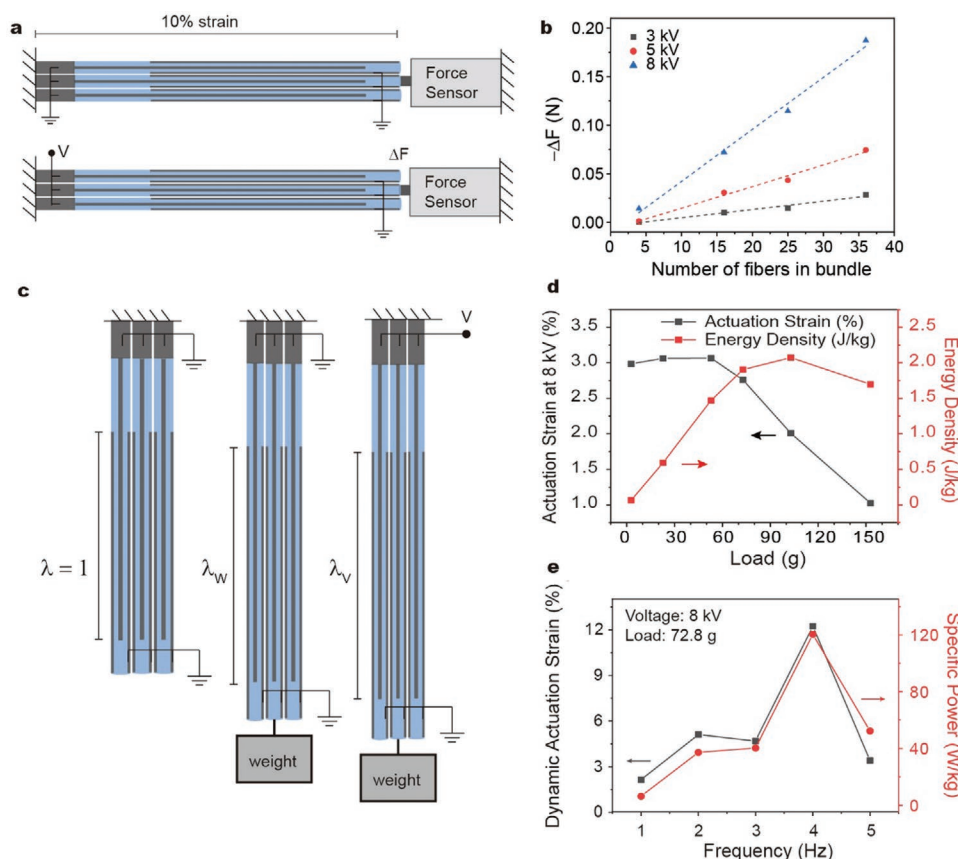


Figure 4. Actuation performance of DEF bundles. a) Schematic view of the restraining force measurement for a DEF bundle, b) restraining force as a function of the number of fibers in the DEF bundle, c) schematic view of the free displacement measurement of DEFs under load, d) maximum actuation strain and mechanical energy density as a function of load for a 5×5 DEF bundle actuated at 8 kV, and e) dynamic actuation strain and specific power of a 5×5 DEF bundle actuated at different frequencies at a peak voltage of 8 kV.

the active fiber (Note S2, Supporting Information), indicating that the RC time constant will limit the actuation frequencies at much larger fiber lengths. At resonance, the actuator operated for over 2.6 million cycles without drift or degradation in the actuation performance (Figure 5c). We note that this combination of fast response and long lifetime is crucial for emerging applications such as flying robots and haptic devices. We also created vertical coils with varying wall thickness of 1, 3, and 5 fiber diameters (Figure 5d). Although the printed coils exhibit uniform displacement during actuation (Figure 5e), their blocked force increases with wall thickness (Figure 5f).

To demonstrate design flexibility and programmed shape-morphing, we created Janus vertical coil actuators by switching the flow of the outer electrode shell ink on and off during 3D printing (Video S2, Supporting Information). Specifically, one side of the vertical coil is printed with DEFs (i.e., with an outer electrode) that can be actuated, while the other side of the coil is printed with fibers that lack an outer electrode. When a voltage is applied, the DEF side contracts, while the other side acts as a passive mechanical constraint, causing the structure to bend in response to a voltage (Figure 5g,h; Video S3, Supporting Information). The off-axis displacement of the Janus coil actuator is shown in Figure 5i. Although we only achieve a

modest displacement of 300 μm , this demonstration highlights our ability to print soft actuators with prescribed electrode patterns.

As a final demonstration, we created steerable DEF bundles in which each fiber is individually addressable leading to a dynamically reconfigurable bundle.^[6,74] We first printed a 3×3 DEF bundle (Figure 6; Video S4, Supporting Information). By electrically addressing different groups of three adjacent fibers, the bundle can be steered by bending in eight different directions (Figure 6a,b). The static displacement and blocked force of the bending bundle tip are reported in Figure S11 in the Supporting Information. We also generated a dynamic response in which the end of this DEF bundle is rotated at 3.125 Hz in a circular pattern by controlling the sequence of electrical signals to individual fibers (Figure 6b–d). These DEF bundles can also exhibit more complex responses, for instance moving in a figure eight pattern, simply by altering the sequence of actuation (Figure 6e). Our dynamically reconfigurable bundles differ from other shape morphing materials,^[18,76] which respond to global stimuli such as temperature or solvent-induced swelling. By contrast these DEF bundles are guided by (in this 3×3 fiber case) nine independently controlled fibers allowing a broad range of programmable actuation states.

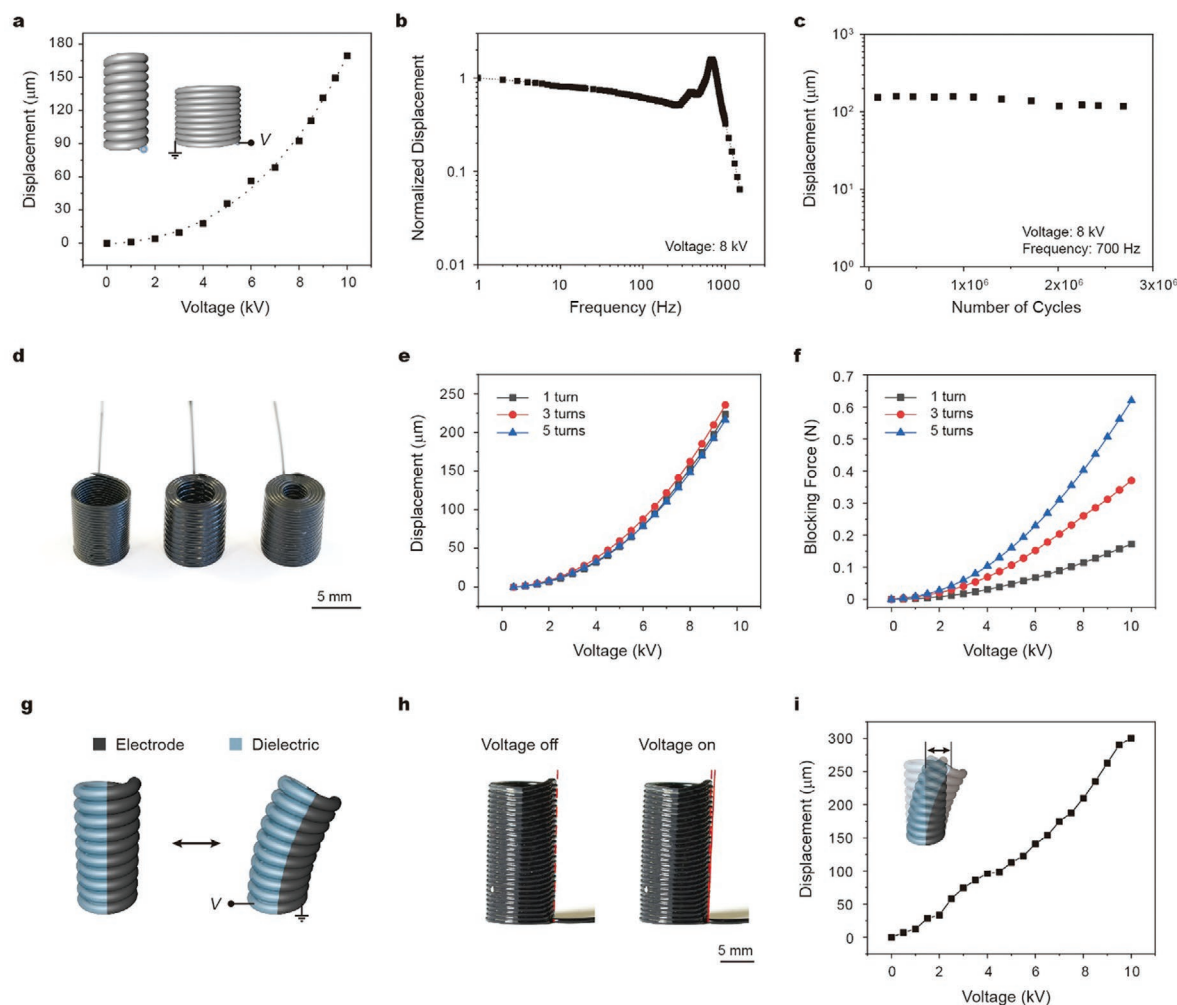


Figure 5. Performance of vertical coil actuators. a) Contractile displacement as a function of voltage, b) normalized contractile displacement as a function of frequency at 8 kV, c) maximum displacement over 2.6 million cycles of vertical coil actuator, d) images of vertical coils consisting of 1, 3, and 5 turns and their e) displacement and f) blocked force as a function of voltage, g) schematic view of a Janus coil actuator, h) image of bending response of a Janus coil actuator, and i) off-axis displacement of a Janus coil actuator as a function of voltage.

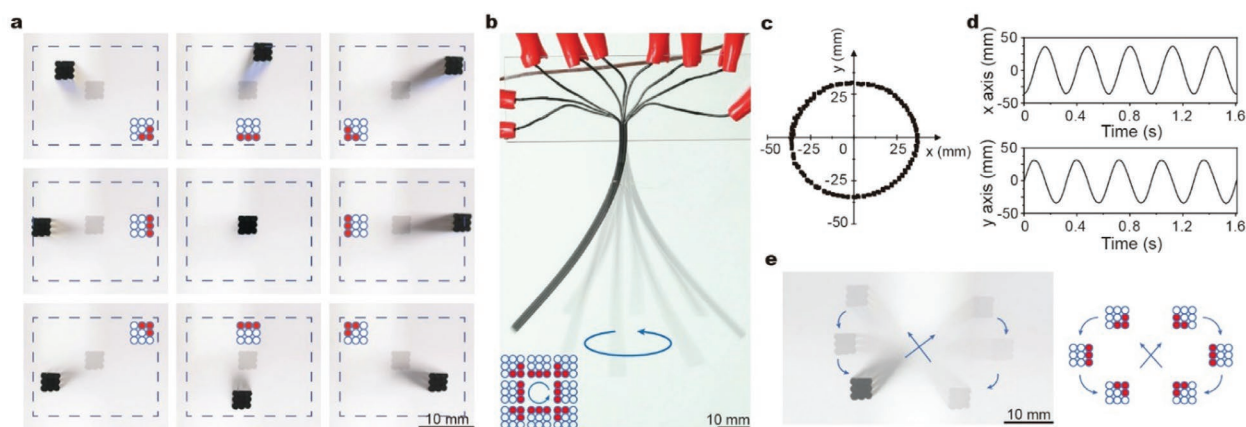


Figure 6. Steerable DEF bundles. a) Bottom view of the end of a 3 × 3 DEF bundle bending in 8 different directions in response to the different addressable actuations shown. The nine circles represent individual fibers and the ones colored red represent those being actuated in each frame. The voltage is 7 kV. The center of each frame is the fixed end of the bundle. b) Side view of the cyclic rotation of the end of this steerable DEF bundle. [Note: The schematic (bottom left) shows the operation sequence for each cycle.] c) and d) Tracking data for the end of the DEF bundle as it rotates in response to a sinusoidal signal. e) The end of the DEF bundle actuated to move in a figure eight pattern, along with a schematic (right) of the addressable sequence used to generate this response.

3. Conclusions

We have created dielectric elastomer fibers, vertical coils, and bundles with programmable shape changes via multimaterial, multicore shell 3D printing. Dielectric matrix and electrode inks were designed with the requisite viscoelastic properties for printing along with optimized mechanical and electrical properties in the printed and cured state. Using this technique, symmetric and asymmetric (Janus) vertical coils were generated with precisely patterned active and non-active regions as well as steerable DEF bundles with individually addressable fibers. With future refinements in both materials and nozzle designs, we anticipate that their actuations strains will be further improved. The ability to actuate DEF devices at their mechanical resonance frequency is crucial for achieving efficient, large-amplitude actuation responses, akin to both biological and engineered systems including human walking gait,^[78] flying microrobots^[72] and tensegrity robots.^[79] Looking ahead, our multimaterial, multicore shell printing method is broadly applicable for fabricating a broad range of soft active materials with integrated functional elements.

4. Experimental Section

Dielectric Ink: Fumed silica nanoparticles (CAB-O-SIL TS-720, from Cabot Corp.) were dispersed in Ecoflex 00-30 (Eco30) part A (Eco30A) and part B (Eco30B) separately by mixing in a SpeedMixer (Flack Tek, Inc) at 2000 rpm for 18 min. 12 g of the Eco30B/silica mixture was weighed into a separate container and 0.36 g (3 wt%) of SloJo cure retarder was added and mixed for another 2 min. 12 g of the Eco30A/silica mixture was added to the container. Finally, 8 g of SE 1700 (Dow Corning Corp.) base and 0.266 g of SE1700 curing agent were added to create a final composition with a weight ratio of 3:1 Eco30:SE1700 and 30:1 SE1700 base:SE1700 curing agent. The composition was mixed at 2000 rpm for 12 min in a SpeedMixer. The resulting dielectric composition included 7.88 wt% TS-720 silica, 32.8 wt% Eco30A, 32.8 wt% Eco30B, 24.5 wt% SE1700 base, 0.82 wt% SE1700 curing agent, and 1.10 wt% SloJo. To improve the dispersion of the nanoparticles, the dielectric ink was roll milled (Torrey Hill, T50) three times. The ink was loaded into 20 cc syringes and centrifuged at 4000 RPM for 20 min to remove any trapped air. Rheology measurements were performed on an AR-2000EX shear rheometer at 25 °C using stainless steel parallel plates with a diameter of 40 mm and a gap of 0.3 mm. After lowering the top plate to the target gap, the sample was allowed to settle for 300 s before starting the measurement. Oscillatory measurements were carried out at a frequency of 1 Hz over a range of shear stress from 1 to 10 000 Pa. Cured dielectric matrices were characterized by shear dynamic mechanical analysis (DMA) using an AR-2000EX rheometer. Samples of uncured dielectric matrix were loaded into the rheometer equipped with a 20 mm steel plate with a gap of 0.3 mm. The samples were heated to 100 °C while collecting oscillation measurements at 1 Hz to monitor the curing. After fully curing, samples were cooled to 25 °C and shear DMA was carried out at a strain of 1% over a frequency range from 0.1 to 100 Hz. Parallel plate capacitors were prepared by blade coating the dielectric ink onto ITO-coated PET. The dielectric ink was cured at 80 °C for 12 h. Gold particles were used to define top electrodes with a diameter of 1 cm. Capacitance measurements were collected using an Agilent E 4980A using controlled using a Labview program.

Electrode Ink: Carbon black nanoparticles (AB100, from Soltex, Inc.) were weighed into Eco30A and Eco30B separately at a content of 13.8 wt%. The compositions were mixed at 2000 rpm for 18 min using a SpeedMixer (Flack Tek, Inc). 12 g of Eco30B/AB100 mixture was

combined with 0.12 g (1 wt%) of SloJo curing retarder and mixed for another 2 min. 12 g of Eco30A/AB100 was added and mixed at 2000 rpm for 12 min in a SpeedMixer, followed by roll milling three times. The dielectric ink was loaded into 20 cc syringes and centrifuged at 4000 RPM for 20 min to remove any trapped air. Rheology measurements were performed on an AR-2000EX shear rheometer at 25 °C using stainless steel parallel plates with a diameter of 40 mm and a gap of 0.3 mm. After lowering the top plate to the target gap, the sample was allowed to settle for 300 s before starting the measurement. Oscillatory measurements were carried out at a frequency of 1 Hz over a range of shear stress from 1 to 10 000 Pa.

Mechanical Testing: Samples of the dielectric and electrode elastomer for tensile testing were printed into rectangular planar sheets with dimensions of 0.8 mm × 60 mm × 60 mm. After curing, the sheets were cut into dog-bone shapes following the ASTM D412a standard scaled down by 2.5 times. Specimens were stretched until rupture on a home-made stretcher (Mint, Baldor) with a load cell (FUTEK LSB200, 2 lb, JR S-Beam Load Cell) at a strain rate of 0.1 s⁻¹. Data was acquired using a LabVIEW program. For electrode inks, the resistance was measured by a Keithley 2636A connected to the two metal clamps of the stretcher. The measuring voltage was 1 V.

Device Fabrication: A multicore-shell nozzle (Figure S3a,b, Supporting Information) was prepared by an Aureus Plus 3D printer with a layer height of 25 μm and an X-Y resolution of 43 μm, as described in the previous work.^[41] The nozzle, dielectric, and electrode inks were mounted to an Aerotech 3-axis stage (Aerotech, Inc.). The pressure of each channel in the nozzle could be controlled by an Ultimius V pressure pump (Nordson EFD) and switched on and off by a solenoid valve while printing (Figure S3c, Supporting Information). The relative dimensions of the DEF samples were printed onto glass plates covered with a Teflon adhesive film (Bytac, Saint-Gobain). Because the ink rheology was temperature-dependent, quickly increasing the curing temperature leads to a viscosity reduction that causes the printed structures to sag under their own weight. Hence, printed samples were first cured at a low temperature of 60 °C for 24 h to drive solidification, followed by curing for 24 h at 80 °C, and finally for 24 h at 110 °C to achieve a fully cured state.

Device Testing: Single fibers were clamped onto a rectangular acrylic frame using conductive copper alligator clips (Figure S6a, Supporting Information). A LabVIEW program increased the voltage at a ramp rate of 100 V s⁻¹ (Bertan 230-30R high voltage source) while recording the deformation of the fiber using a Point Grey automation camera. To test the restraining force of the bundle actuators, the bundles were secured at 10% strain in a linear stage equipped with a load cell (FUTEK LSB200, 2 lb., JR S-Beam). A LabVIEW program increased the voltage at a rate of 100 V s⁻¹ while monitoring the force. The change in force was referred to as the restraining force. Free displacement of bundles was measured by clamping the top of a bundle and securing a weight to the bottom of a bundle using a binder clip. A LabVIEW program controlled the voltage through a Trek 610E amplifier. The quasi-static actuation behavior was measured by increasing the voltage in steps of 0.5 up to 8 kV and the deformation was captured using a Sony α7 II camera. The dynamic response of the loaded bundles was captured by a high-speed camera (FASTCAM Mini AX, Photron USA, Inc). The position, velocity and acceleration of the load was determined from video recordings using analysis software (Tracker). The power output ($P(t)$) of the bundle actuators for lifting a mass (m) were calculated by the time-derivative of the sum of potential (PE) and kinetic energy (KE) of the mass (m)

$$P(t) = \frac{d(KE)}{dt} + \frac{d(PE)}{dt} = \frac{d\left(\frac{1}{2}mv(t)^2\right)}{dt} + \frac{d(mgy(t))}{dt} = mv(t)[a(t) + g] \quad (2)$$

where $y(t)$ is the vertical position, $v(t)$ is the velocity of the mass, $a(t)$ is its acceleration, and g is the gravitational acceleration. The gravimetric work was calculated by integrating the power over time during contraction. The specific power was calculated as the maximum instantaneous power divided by the weight of the actuator.

The actuation of vertical coil actuators was measured using a LabVIEW program that controlled the output voltage of a high voltage supply (Trek 610E) and recorded the displacement using a non-contact optical sensor (2100 Fotonics Sensor, MTI Instruments, Inc). The frequency response and cycling behavior were measured using a sine wave with minimum and maximum voltages of 0 and 8 kV. The cycling measurement was carried out at 700 Hz. Blocked force measurements were carried out with a compressive preload of 800 mN, and a load cell (FUTEK LSB200, 2 lb, JR S-Beam load cell) measured the force as a function of voltage.

To individually address each fiber actuator in the steerable bundle, a switching circuit was built which consisted of several relays and transistors (Figure S11, Supporting Information) using a data acquisition device (NI DAQ USB-6003) to interface with a LabVIEW program. The LabVIEW program controlled the voltage of the power supply (Trek 610E) as well as the switching of relays that turned on or off the voltage to each fiber. The capacitance versus frequency was measured using an LCR meter (Agilent E4980A) controlled with a LabVIEW program.

Supporting Information

Supporting Information is available from the Wiley Online Library or from the author.

Acknowledgements

A.C. and J.M. contributed equally to this work. This work is supported by the Harvard MRSEC program of the National Science Foundation under award number DMR 20-11754.

Conflict of Interest

J.A. Lewis is a co-founder of Voxel8, Inc., a multimaterial 3D printing company.

Data Availability Statement

The data that support the findings of this study are available from the corresponding author upon reasonable request.

Keywords

3D printing, dielectric elastomer actuators, soft robotics

Received: December 10, 2020

Revised: February 18, 2021

Published online:

- [1] A. Kotikian, R. L. Truby, J. W. Boley, T. J. White, J. A. Lewis, *Adv. Mater.* **2018**, 30, 1706164.
- [2] Y. Kim, H. Yuk, R. Zhao, S. A. Chester, X. Zhao, *Nature* **2018**, 558, 274.
- [3] H. Arazoe, D. Miyajima, K. Akaike, F. Araoka, E. Sato, T. Hikima, M. Kawamoto, T. Aida, *Nat. Mater.* **2016**, 15, 1084.
- [4] E. Acome, S. K. Mitchell, T. G. Morrissey, M. B. Emmett, C. Benjamin, M. King, M. Radakovitz, C. Keplinger, *Science* **2018**, 359, 61.

- [5] M. Kanik, S. Orguc, G. Varnavides, J. Kim, T. Benavides, D. Gonzalez, T. Akintilo, C. C. Tasan, A. P. Chandrakasan, Y. Fink, P. Anikeeva, *Science* **2019**, 365, 145.
- [6] M. Duduta, E. Hajiesmaili, H. Zhao, R. J. Wood, D. R. Clarke, *Proc. Natl. Acad. Sci. USA* **2019**, 116, 2476.
- [7] A. S. Gladman, E. A. Matsumoto, R. G. Nuzzo, L. Mahadevan, J. A. Lewis, *Nat. Mater.* **2016**, 15, 413.
- [8] E. Hajiesmaili, D. R. Clarke, *Nat. Commun.* **2019**, 10, 183.
- [9] A. Sidorenko, T. Krupenkin, A. Taylor, P. Fratzl, J. Aizenberg, *Science* **2007**, 315, 487.
- [10] S. M. Mirvakili, I. W. Hunter, *Adv. Mater.* **2018**, 30, 1704407.
- [11] E. Siefert, E. Reyssat, J. Bico, B. Roman, *Nat. Mater.* **2019**, 18, 24.
- [12] Y. L. Yu, M. Nakano, T. Ikeda, *Nature* **2003**, 425, 145.
- [13] S. Li, H. Bai, R. F. Shepherd, H. Zhao, *Angew. Chem., Int. Ed.* **2019**, 58, 11182.
- [14] C. P. Ambulo, J. J. Burroughs, J. M. Boothby, H. Kim, M. R. Shankar, T. H. Ware, *ACS Appl. Mater. Interfaces* **2017**, 9, 37332.
- [15] P. Polygerinos, Z. Wang, K. C. Galloway, R. J. Wood, C. J. Walsh, *Rob. Auton. Syst.* **2015**, 73, 135.
- [16] F. Connolly, C. J. Walsh, K. Bertoldi, *Proc. Natl. Acad. Sci. USA* **2017**, 114, 51.
- [17] M. Schaffner, J. A. Faber, L. Pianegonda, P. A. Rühs, F. Coulter, A. R. Studart, *Nat. Commun.* **2018**, 9, 878.
- [18] J. W. Boley, W. M. van Rees, C. Lissandrello, M. N. Horenstein, R. L. Truby, A. Kotikian, J. A. Lewis, L. Mahadevan, *Proc. Natl. Acad. Sci. USA* **2019**, 116, 20856.
- [19] Y. Jiang, L. M. Korpas, J. R. Raney, *Nat. Commun.* **2019**, 10, 128.
- [20] A. Kotikian, C. McMahan, E. C. Davidson, J. M. Muhammad, R. D. Weeks, C. Daraio, J. A. Lewis, *Sci. Robot.* **2019**, 4, eaax7044.
- [21] Y. Dong, J. Wang, X. Guo, S. Yang, M. O. Ozen, P. Chen, X. Liu, W. Du, F. Xiao, U. Demirci, *Nat. Commun.* **2019**, 10, 4087.
- [22] H. Shahsavan, A. Aghakhani, H. Zeng, Y. Guo, Z. S. Davidson, A. Priimagi, M. Sitti, *Proc. Natl. Acad. Sci. USA* **2020**, 117, 5125.
- [23] Y. Zhao, C. Xuan, X. Qian, Y. Alsaid, M. Hua, L. Jin, X. He, *Sci. Robot.* **2019**, 4, eaax7112.
- [24] Y.-c. Chang, W.-j. Kim, *IEEE/ASME Trans. Mechatronics* **2012**, 18, 547.
- [25] X. H. Zhao, Z. G. Suo, *Phys. Rev. Lett.* **2010**, 104, 178302.
- [26] R. Pelrine, R. Kornbluh, Q. B. Pei, J. Joseph, *Science* **2000**, 287, 836.
- [27] Z. Xing, J. Zhang, D. McCoul, Y. Cui, L. Sun, J. Zhao, *Soft Robot.* **2020**, 7, 512.
- [28] A. Marette, A. Poulin, N. Besse, S. Rosset, D. Briand, H. Shea, *Adv. Mater.* **2017**, 29, 1700880.
- [29] A. Chortos, E. Hajiesmaili, J. Morales, D. R. Clarke, J. A. Lewis, *Adv. Funct. Mater.* **2020**, 30, 1907375.
- [30] X. Ji, X. Liu, V. Cacucciolo, M. Imboden, Y. Civet, A. El Haitami, S. Cantin, Y. Perriard, H. Shea, *Sci. Rob.* **2019**, 4, eaaz6451.
- [31] M. Hamed, L. Herlogsson, X. Crispin, R. Marcilla, M. Berggren, O. Inganäs, *Adv. Mater.* **2009**, 21, 573.
- [32] J. Maas, D. Tepel, T. Hoffstadt, *Meccanica* **2015**, 50, 2839.
- [33] G. Haghighatshani, E. Habtour, S.-H. Park, F. Gardea, M. C. McAlpine, *Extreme Mech. Lett.* **2018**, 21, 1.
- [34] O. Araromi, A. Conn, C. Ling, J. Rossiter, R. Vaidyanathan, S. Burgess, *Sens. Actuators, A* **2011**, 167, 459.
- [35] A. H. Zamanian, D. A. Porter, P. Krueger, E. Richer, presented at ASME 2018 Dynamic Syst. and Control Conf., Atlanta, GA, November **2018**.
- [36] C. A. Manion, D. K. Patel, M. Fuge, S. Bergbrieter, in *IEEE/RSJ Int. Conf. Intell. Robots Syst. (IROS)*, IEEE, Piscataway, NJ **2018**.
- [37] M. R. O'Neill, E. Acome, S. Bakarich, S. K. Mitchell, J. Timko, C. Keplinger, R. F. Shepherd, *Adv. Funct. Mater.* **2020**, 30, 2005244.
- [38] N. Zhou, C. Liu, J. A. Lewis, D. Ham, *Adv. Mater.* **2017**, 29, 1605198.
- [39] M. A. Skylar-Scott, J. Mueller, C. W. Visser, J. A. Lewis, *Nature* **2019**, 575, 330.
- [40] V. G. Rocha, E. Saiz, I. S. Tirichenko, E. García-Tuñón, *J. Mater. Chem. A* **2020**, 8, 15646.

- [41] J. Mueller, J. R. Raney, K. Shea, J. A. Lewis, *Adv. Mater.* **2018**, 30, 1705001.
- [42] A. Frutiger, J. T. Muth, D. M. Vogt, Y. Mengüç, A. Campo, A. D. Valentine, C. J. Walsh, J. A. Lewis, *Adv. Mater.* **2015**, 27, 2440.
- [43] R. E. Pelrine, R. D. Kornbluh, J. P. Joseph, *Sens. Actuators, A* **1998**, 64, 77.
- [44] F. Carpi, D. De Rossi, *Mater. Sci. Eng., C* **2004**, 24, 555.
- [45] S. Arora, T. Ghosh, J. Muth, *Sens. Actuators, A* **2007**, 136, 321.
- [46] C. G. Cameron, J. P. Szabo, S. Johnstone, J. Massey, J. Leidner, *Sens. Actuators, A* **2008**, 147, 286.
- [47] J. Zhu, H. Stoyanov, G. Kofod, Z. Suo, *J. Appl. Phys.* **2010**, 108, 074113.
- [48] G. Kofod, H. Stoyanov, R. Gerhard, *Appl. Phys. A: Mater. Sci. Process.* **2011**, 102, 577.
- [49] R. B. Rao, K. L. Krafcik, A. M. Morales, J. A. Lewis, *Adv. Mater.* **2005**, 17, 289.
- [50] R. L. Truby, J. A. Lewis, *Nature* **2016**, 540, 371.
- [51] F. B. Madsen, A. E. Daugaard, S. Hvilsted, A. L. Skov, *Macromol. Rapid Commun.* **2016**, 37, 378.
- [52] D. Kong, R. Pfattner, A. Chortos, C. Lu, A. C. Hinckley, C. Wang, W. Y. Lee, J. W. Chung, Z. Bao, *Adv. Funct. Mater.* **2016**, 26, 4680.
- [53] K.-Y. Chun, Y. Oh, J. Rho, J.-H. Ahn, Y.-J. Kim, H. R. Choi, S. Baik, *Nat. Nanotechnol.* **2010**, 5, 853.
- [54] M. L. Hammock, A. Chortos, B. C. K. Tee, J. B. H. Tok, Z. Bao, *Adv. Mater.* **2013**, 25, 5997.
- [55] S. Gong, W. Cheng, *Adv. Electron. Mater.* **2017**, 3, 1600314.
- [56] J. D. Davidson, N. Goulbourne, *J. Mech. Phys. Solids* **2013**, 61, 1784.
- [57] N. Goulbourne, E. Mockensturm, M. Frecker, *J. Appl. Mech.* **2005**, 72, 899.
- [58] R. A. Toupin, *Arch. Ration. Mech. Anal.* **1956**, 5, 849.
- [59] J. Zhu, S. Cai, Z. Suo, *Int. J. Solids Struct.* **2010**, 47, 3254.
- [60] Z. Suo, *Acta Mech. Solida Sin.* **2010**, 23, 549.
- [61] J.-S. Plante, S. Dubowsky, *Int. J. Solids Struct.* **2006**, 43, 7727.
- [62] X. Zhao, Z. Suo, *Appl. Phys. Lett.* **2007**, 91, 061921.
- [63] D. M. Opris, *Adv. Mater.* **2018**, 30, 1703678.
- [64] L. Yu, A. L. Skov, *Macromol. Rapid Commun.* **2018**, 39, 1800383.
- [65] Y. Sheima, P. Caspari, D. M. Opris, *Macromol. Rapid Commun.* **2019**, 40, 1900205.
- [66] C. Yuan, Y. Zhou, Y. Zhu, J. Liang, S. Wang, S. Peng, Y. Li, S. Cheng, M. Yang, J. Hu, B. Zhang, R. Zeng, J. He, Q. Li, *Nat. Commun.* **2020**, 11, 3919.
- [67] C. B. Gale, M. A. Brook, A. L. Skov, *RSC Adv.* **2020**, 10, 18477.
- [68] C. S. O'Bryan, T. Bhattacharjee, S. Hart, C. P. Kabb, K. D. Schulze, I. Chilakala, B. S. Sumerlin, W. G. Sawyer, T. E. Angelini, *Sci. Adv.* **2017**, 3, 1602800.
- [69] R. Xie, S. Mukherjee, A. E. Levi, V. G. Reynolds, H. Wang, M. L. Chabinyc, C. M. Bates, *Sci. Adv.* **2020**, 6, eabc6900.
- [70] T. J. Hinton, A. Hudson, K. Pusch, A. Lee, A. W. Feinberg, *ACS Biomater. Sci. Eng.* **2016**, 2, 1781.
- [71] H. C. Zhao, A. M. Hussain, M. Duduta, D. M. Vogt, R. J. Wood, D. R. Clarke, *Adv. Funct. Mater.* **2018**, 28, 1804328.
- [72] Y. Chen, H. Zhao, J. Mao, P. Chirarattananon, E. F. Helbling, N.-s. P. Hyun, D. R. Clarke, R. J. Wood, *Nature* **2019**, 575, 324.
- [73] J. Zhang, J. Sheng, C. T. O'Neill, C. J. Walsh, R. J. Wood, J.-H. Ryu, J. P. Desai, M. C. Yip, *IEEE Trans. Rob.* **2019**, 35, 761.
- [74] Q. He, Z. Wang, Y. Wang, A. Minori, M. T. Tolley, S. Cai, *Sci. Adv.* **2019**, 5, eaax5746.
- [75] E. Leroy, R. Hinchet, H. Shea, *Adv. Mater.* **2020**, 32, 2002564.
- [76] C. Huang, Z. Wang, D. Quinn, S. Suresh, K. J. Hsia, *Proc. Natl. Acad. Sci. USA* **2018**, 115, 12359.
- [77] H. Y. Jeong, E. Lee, S. Ha, N. Kim, Y. C. Jun, *Adv. Mater. Technol.* **2019**, 4, 1800495.
- [78] M. Lee, S. Kim, S. Park, *J. Biomech.* **2014**, 47, 319.
- [79] T. Bliss, T. Iwasaki, H. Bart-Smith, *IEEE/ASME Trans. Mechatronics* **2012**, 18, 586.